Three-periodic 1D photonic crystals for designing the photonic optical devices operating in the infrared regime

Ivan Panyaev, Dmitry Sannikov, Nataliya Dadoenkova, Yuliya Dadoenkova

Three-periodic 1D photonic crystals for designing the photonic optical devices operating in the infrared regime

IVAN S. PANYAEV,[1] DMITRY G. SANNIKOV,[1,*] NATALIYA N. DADOENKOVA,[1,2] YULIYA S. DADOENKOVA[3,+]

[1]*Ulyanovsk State University, Ulyanovsk 432017, Russia*
[2]*Donetsk Institute for Physics and Engineering named after A. A. Galkin, Donetsk, Ukraine*
[3]*Lab-STICC (UMR 6285), CNRS, ENIB, 29238 Brest Cedex 3, France*
[+]*Also associated with Ulyanovsk State University, Ulyanovsk 432017, Russia*
**Corresponding author: sannikov-dg@yandex.ru*

Received XX Month XXXX; revised XX Month, XXXX; accepted XX Month XXXX; posted XX Month XXXX (Doc. ID XXXXX); published XX Month XXXX

We investigate theoretically and numerically one-dimensional three-periodic photonic crystals of the structure $[(SiO_2/TiO_2)^N(Al_2O_3/ZrO_2)^M]^K$, formed by dielectric oxides SiO_2, TiO_2, Al_2O_3, and ZrO_2 (N and M are the number of subperiods, and K is the number of superperiods). We study the transmission spectra, energy and power fluxes of TE- and TM-polarised electromagnetic waves for a photonic crystal, characterized by the sharp photonic bandgap edges, narrow and pronounced peaks of defect modes. The angular distance (difference in the incidence angles) between the transmission peaks of different polarizations is shown to be about 1.5 degrees that is five times more than in the ternary photonic crystals. The results can be useful for designing highly efficient optical devices operating in the infrared regime on the side-surface of the photonic crystal, such as polarization-sensitive couplers and angle sensors for the optical fiber systems, etc.

1. INTRODUCTION

During two last decades, one-dimensional (1D) photonic crystals (PC) have been successfully implemented in various photonic and optoelectronic devices: solar cells, sensors, 3D matrices, fluorescent amplifying devices, color displays, sensors, etc. [1–3]. The possibility of the distributed-feedback laser structures fabrication using a 1D PC is currently discussed [4].

The presence of defect modes within the photonic band gap (PBG) of such structures allows them to be used, for instance, in various fields of medicine. Methods for detecting a cancer cell and brain lesions by recording the shift of the transmission peaks in a 1D photonic structures were proposed [5,6]. To detect the hemoglobin level, 1D binary PCs containing a defect layer are used due to strong dependence of the resonant peaks in the PBG on the concentration and the consequent refractive index [7]. 1D PC can also be used in stealth technologies [8].

It has been shown that 1D PCs can be used for thermophotovoltaic applications [9]. Being conjugated with a liquid-crystal anisotropic defect layer and covered by a metal film, 1D PC can support localized solutions that correspond to isolated discrete eigenvalues, which can be used in novel tunable high-quality devices both in spintronics and photonics [10]. Typically, in PC design the PBG with well-defined center and edge frequencies is desirable. To expand the PBG, a technique based on mixing the PCs with different lattice constants or filling factors is proposed [11]. Special attention should be paid to the so-called pseudo-periodic, disordered and deterministic aperiodic 1D PCs. They were proposed to be used, for example, to expand the high-reflection range in the visible and near-IR spectral regimes while maintaining an ultra-narrow bandpass [12], or to create polarization-sensitive dichroic filters [13].

In series of publications, multiperiodic functional materials based 1D PCs are proposed as a basis for modern integrated photonics: complex devices based on magneto-optic waveguides and a PC [14]. It is also shown that these structures can find their applications in the photonic devices controlled by the external fields [15], in designing the asymmetric and bidirectional nanophotonic devices which are used for the signal modulation/switching [16] and for the fabrication of highly

efficient optical devices (optical switchers, filters, splitters, etc.) of the IR range [17].

Photonic structure with two periods where the internal finite-size block (ab)N is inside the unit cell [(ab)Nc] repeated M times were considered as photonic–magnonic crystals [18–22] and were studied as photonic hypercrystals [23–26]. In Ref. [27], the intraband (defect) modes in the transmission spectra in the near-IR range are studied, as well as their number and resonance frequencies, which can be adjusted by changing the parameters of the structure and incidence angle of the electromagnetic radiation. It was proposed to use these structures in the design of efficient optical filters and highly sensitive angular sensors (optical filters with high selectivity, coatings, ultra-sensitive angular sensors, etc.) operating in the optical and infrared regimes. In paper [28], a ternary (Si/polymer/SiO2) PC was proposed as a temperature sensor. The operation principle of the proposed device is based on the red shift of the transmission peak with an increase of the temperature due to the influence of thermooptical and thermal expansion coefficients of the polymer. Similarly, 1D phoxonic crystal chemical sensors have been discussed in [29]. A ternary PC containing a superconductor has a similar operating principle [30]. When considering biosensors based on 1D PC, more than a two-fold improvement in volumetric and surface sensitivity is achieved in comparison with conventional micromirror sensors [31]. 1D ternary PCs can serve as highly sensitive defect mode refractometric sensors [32]. Ternary structures based on bi-periodic magneto-optic planar PCs can also be implemented in the lower frequency region [33].

In this paper, we theoretically investigate three-periodic 1D PCs, consisting of four dielectric oxides with different refractive indices. We continue our study started in Ref. [34], where 1D three-periodic PCs with different order of layers are classified according to the magnitude and sign of optical contrast. The novelty of this paper consists in calculations of energy fluxes through the structure and analysis of the energy distribution of a light wave within the PC composed of a specific arrangement of alternating high- and low-optical-contrast subcells. We also discuss the prospects of using this type of PC structures for fabrication of precision polarization-sensitive sensors, input-output devices for electromagnetic radiation into an optical fiber through the side surface of the PC, and other applications in nanophotonics and optoelectronics.

2. GEOMETRY OF THE SYSTEM

Let us consider a four-component three-periodic PC of the structure $[(ST)^N(AZ)^M]^K$, where S, T, A and Z denote the silicon oxide (SiO_2), titanium oxide (TiO_2), aluminum (Al_2O_3), and zirconium oxide (ZrO_2) layers with the corresponding thicknesses l_S, l_T, l_A, and l_Z, as shown in Fig. 1. All the materials are technologically compatible with each other [35]. Two subcells $(ST)^N$ and $(AZ)^M$ are 1D finite two-component single-periodic PCs with the periods $L_1 = l_S + l_T$ and $L_2 = l_A + l_Z$, respectively. They form the supercell of the three-periodic PC with the super-period $L_3 = NL_1 + ML_2$. The total thickness of the structure is thus equal to $L = KL_3$.

A near-infrared monochromatic wave of wavelength λ in an air is incident on the left-hand side of the PC under an angle θ, so that the (xz) is the incidence plane. We assume that the longitudinal dimensions along the x- and y-directions are large enough to neglect the corresponding boundary effects.

We restrict our consideration of the incident electromagnetic waves within the wavelength range λ = (1 - 5) μm. In the considered regime, all the chosen materials are transparent, and have refractive indices $n_j(\mu)$ (j = S, T, A, Z) which vary monotonously with angular frequency μl and $n_T > n_Z > n_A > n_S$ [34]. In this case, the eigenmodes of the PC are TE- and TM-polarized waves. We take into account the frequency dispersion of all the refractive indices via the Sellmeier equations [36–39]. The unit cell (ST) is characterized by a high value of optical contrast $\Delta n_{ST} = n_S - n_T$ between the materials S and T, and the unit cell (AZ) has a low optical contrast $\Delta n_{AZ} = n_A - n_Z$ between the layers A and Z. According to the classification of the four-component three-periodic PCs, proposed in [34], such structure belongs to the group $\boldsymbol{h}^{-}\boldsymbol{l}^{-}$, where $\boldsymbol{h}$ and $\boldsymbol{l}$ refer to the high and low optical contrast, respectively (superscript "–" refer to its sign), and the spectra of such PCs possess pronounced wide PBGs with clear boundaries.

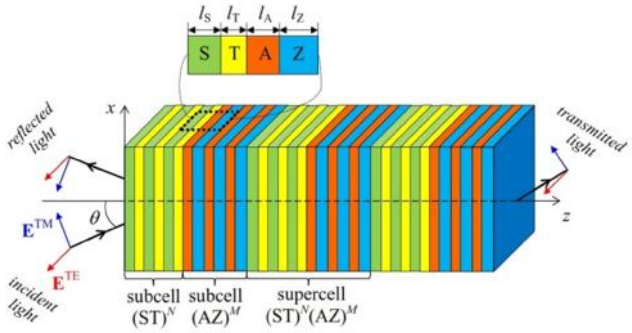

Fig. 1. Schematic of 1D dielectric three-periodic PC of the structure $[(ST)^N(AZ)^M]^K$. Here $\mathbf{E}^{TE}$ and $\mathbf{E}^{TM}$ denote electric field of TE- and TM-polarized electromagnetic waves, and θ is the incidence angle.

The transmission spectra of 1D PCs are known to be generally determined by the refractive indices and thicknesses of the layers of the structure [40–42]. These parameters are related through the Bragg condition of the equal optical paths in each layer: $n_j l_j = a_0/4$. Note that in this case a_0 corresponds to the PBG center of the PC formed by the periodic repetitions of whatever pairs of these layers.

The thicknesses of the layers satisfying the Bragg condition are illustrated in Fig. 2 as functions of a_0. One can see that the thickness of each quarter-wavelength layer increases with the increase of the chosen PBG center a_0. Moreover, the difference between the thicknesses of the quarter-wavelength layers, constituting the structure, increases due to the frequency dispersion of the refractive indices. It should be noted that at the fixed wavelength a_0, the less optically dense layers have larger thicknesses to satisfy the Bragg condition. In this paper, we consider the three-periodic PC with the fixed but different PBG centers of the high- and low-optical-contrast subcells denoted a_{0h} and a_{0l}, respectively. Thus, the thicknesses of the layers are adjusted to the chosen wavelengths of the subcell PBG centers and are defined via the Bragg condition as

$$l_{S,T} = \frac{a_{0h}}{4n_{S,T}(a_{0h})}, \quad l_{A,Z} = \frac{a_{0l}}{4n_{A,Z}(a_{0l})}. \qquad (1)$$

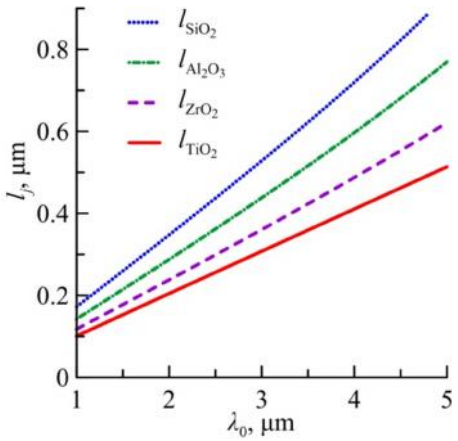

Fig. 2. Quarter-wavelength thicknesses of the PC layers as functions of the wavelength a_0.

3. NUMERICAL RESULTS

For the numerical analysis, unless otherwise stated, we consider the three-periodic structures with the sub- and super-period numbers $M = N = K = 3$ which is enough to obtain pronounced PBGs with vertical edges. The thicknesses of the layers constituting the structure for different PBG centers of the subcells (for Figs. 3-7) are given in Table 1. The total number of the layers is 36.

Table 1. Thicknesses of the layers for the different PBC-centers of the subcells.

a_0	μ_0	ST-subcell		AZ-subcell	
(μm)	(rad·PHz)	l_S (μm)	l_T (μm)	l_A (μm)	l_Z (μm)
1.0	1.885	0.172	0.101	0.142	0.118
1.5	1.257	0.260	0.153	0.215	0.178
2.0	0.942	0.348	0.205	0.288	0.238

A. Transmission spectra

As was shown in Ref. [34], the transmission spectra, the position, width, and sharpness of the PBG edges of the three-periodic PCs strongly depend on the choice of the wavelengths a_{0h} and a_{0l}. Thus, choosing the different values of the PBG centers of the high- and low-optical-contrast subcells, one can significantly modify the spectra of three-periodic PC, as is illustrated in Fig. 3. The upper panel in Fig. 3 (in green) shows the transmission spectra of TE-modes, and the bottom one (in blue) corresponds to the spectra of TM-modes.

The PBG edges of single-periodic PCs formed by the high- and low-optical-contrast subcells $(ST)^9$ (the limiting case of the structure $[(ST)^N(AZ)^M]^K$ with $N = 3$, $M = 0$, $K = 3$) and $(AZ)^9$ (the limiting case with $N = 0$, $M = 3$, $K = 3$) are shown with the yellow dashed and the red dotted lines, respectively. From Fig. 3 one can see that the PBG of the structure with high optical contrast $(ST)^9$ is wider than that of the low-optical-contrast PC $(AZ)^9$. Note that in Figs. 3(a)-3(c) and 3(j)-3(l), only the low-frequency PBG edges of the structure $(ST)^9$ are shown; similarly, in Figs. 3(a), 3(d), 3(g) and 3(j), 3(m), 3(p) the high-frequency edges of the structure $(AZ)^9$ are not shown because they are beyond the considered frequency range.

Previously we have shown that the position of the resulting PBG center of the three-periodic PC is mainly determined by the spectral properties of the high-optical-contrast subcell (see Ref. [34]). Indeed, the PBG centers of the resulting structure $[(ST)^3(AZ)^3]^3$ coincide with those of the PBG of the structure $(ST)^9$, so that the increase of a_{0h} leads to a red shift of the PBG of the three-periodic PC [compare, for instance, Figs. 3(a), 3(d), and 3(g)]. However, the widths of the resulting PBGs are larger in comparison to those of the structure $(ST)^9$, and the intraband modes appear in the spectra as a result of the presence of the low-optical-contrast subcells $(AZ)^3$. These modes can be treated as the defect modes appeared due to the subcells $(AZ)^3$ which act as complex defect layers with respect to the single-periodic structure composed of the high-optical-contrast subcells. The number and the positions of the intraband modes can vary with the wavelength a_{0l} of the PBG center of the subcell $(AZ)^3$. Indeed, the increase of a_{0l} can shorten the frequency distance between the peaks (see, for instance, Figs. 3(d)-3(f) and 3(m)-3(o)) or can produce two intraband modes instead of one (Figs. 3(h), 3(i) and 3(q), 3(r)). This is related to the change of the thicknesses l_A and l_Z of the layers of the low-contrast subcell which satisfy the Bragg condition Eq. (1), and thus to the change of the conditions of the constructive and destructive interference of the waves partially reflected and transmitted at each interface of the structure which determine the existence of the defect modes.

Note that each intraband mode is split into two sub-peaks, which is in a good agreement with the previously shown properties. Indeed, it was shown [43] that the number of the sub-peaks of the intraband mode equals to $(K–1)$. Comparing the obtained transmission spectra with those for biperiodic PCs [18,19,20,22,27,], as well as to the spectra of multiperiodic PCs with more complex structure of the subcells [44], one can say that such a splitting of the intraband modes is a common property of the transmission spectra of all the multiperiodic structures.

When the centers of the PBGs of the high- and low-optical-contrast PCs are the same, *i.e.*, $a_{0h} = a_{0l}$, the resulting PBG of the three-periodic PC is especially well-pronounced in the region between the intraband modes due to an overlap of the PBGs of the structures $(ST)^9$ and $(AZ)^9$. When $a_{0h} \neq a_{0l}$, the minimal values of the transmittivity in the PBGs are slightly larger, and the PBG edges are less sharp. Note that in this case the PBGs are less deep at small incidence angles ¯ for the TE-mode and at large ¯ for the TM-mode.

B. Transverse intensity

The transmittivity spectra ensure the application of the PCs as optical filters within the PBG frequency ranges [45]. On the other hand, peculiarities of the energy characteristics of the multiperiodic structures can open new application possibilities, for instance, for photolithographic purposes [46].

The transverse Umov-Poynting vector components $S_x(z)$, which characterize the energy fluxes (intensities) of the electromagnetic wave within the PC structure along the x-axis and depend on the z-coordinate, are given by

$$S_x^{\mathrm{TE}}(z) = \frac{c}{8®}\mathrm{Re}(E_y H_z^*), \quad S_x^{\mathrm{TM}}(z) = -\frac{c}{8®}\mathrm{Re}(E_z H_y^*) \quad (2)$$

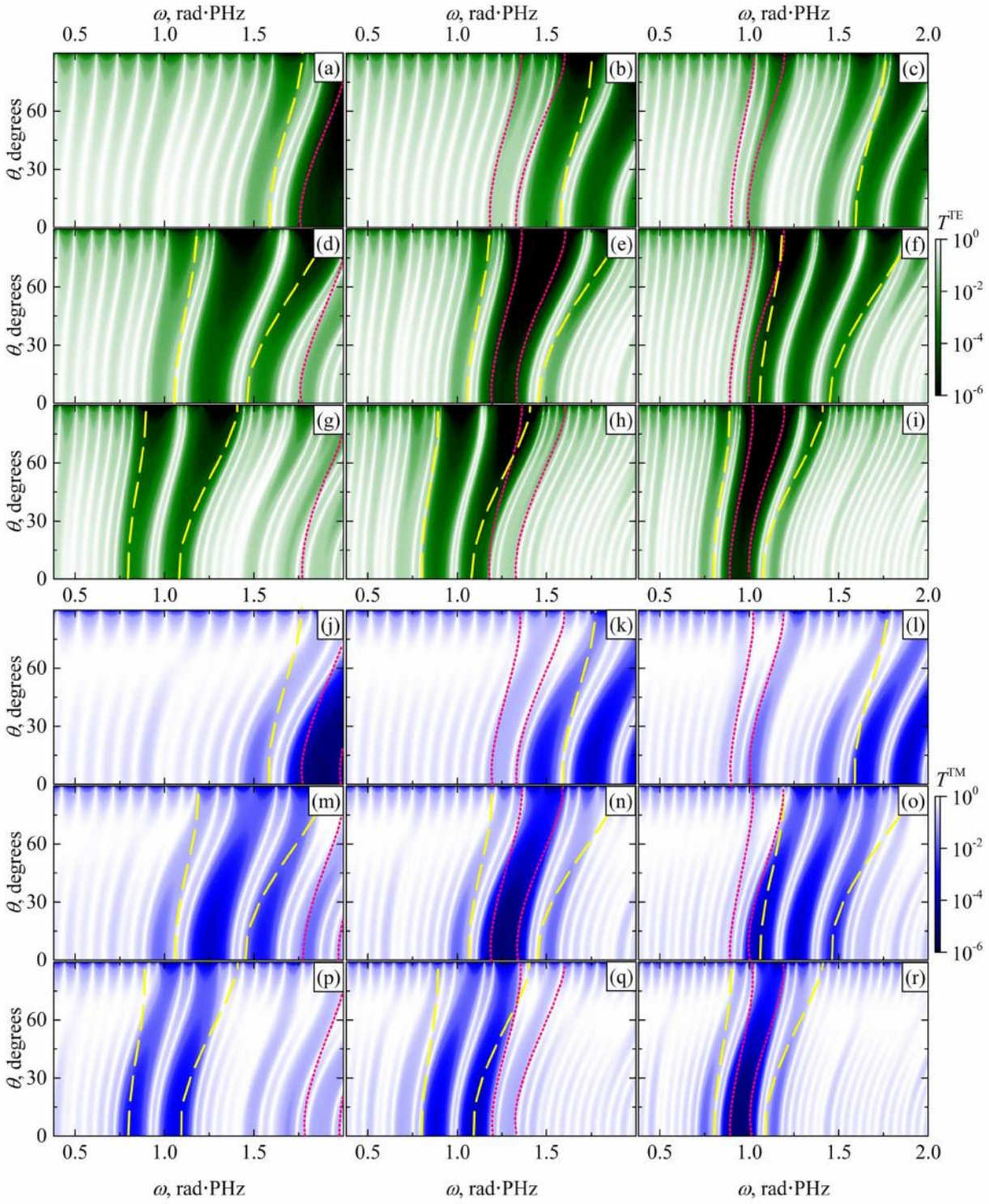

Fig. 3. Transmission spectra $T(\bar{}, \mu)$ of the structure $[(ST)^3(AZ)^3]^3$ for TE- [the top panel (a)-(i)] and TM- [the bottom panel (j)-(r)] modes at various values of a_{0h} and a_{0l}. In the top row, a_{0h} = 1.0 μm (μ_{0h} = 1.885 rad·PHz), in the middle row, a_{0h} = 1.5 μm (μ_{0h} = 1.257 rad·PHz), in the bottom row, a_{0h} = 2.0 μm (μ_{0h} = 0.942 rad·PHz); in the left column, a_{0l} = 1.0 μm, in the middle column, a_{0l} = 1.5 μm, in the right column, a_{0l} = 2.0 μm. The yellow dashed and the red dotted lines show the PBG edges of single-periodic PCs formed by the high- and low-optical-contrast subcells $(ST)^9$ and $(AZ)^9$, respectively.

for TE- and TM-modes, respectively. Here $E_{y,z}$ and $H_{y,z}$ are the components of the electric and magnetic field of the electromagnetic wave, c is the speed of light in the vacuum, and Re and Im refer to the real and imaginary parts of a complex number, respectively.

For calculation of the energy fluxes we use the value of the electric field magnitude (both for TE- and TM-polarized radiation) at the left-hand-side surface of the PC to be $S_0 = 0.03$ $(\text{erg/cm}^3)^{1/2}$ [27], which is in agreement with the conventional values for the He-Ne laser [47].

Figure 4 shows the distribution of the transverse intensity S_x inside the structure $[(ST)^3(AZ)^3]^3$ as function of the incidence angle ¯ (the top panel), and as function of the angular frequency μ for the fixed incidence angle ¯ = 45° (the bottom panel) for TE- and TM- polarizations (the green and purple panels, respectively), in the cases $^{a}_{0h}$ = 1.5 μm and $^{a}_{0l}$ = 2 μm (the first and the second columns), and $^{a}_{0h}$ = 2 μm and $^{a}_{0l}$ = 1.5 μm (the third and the fourth columns).

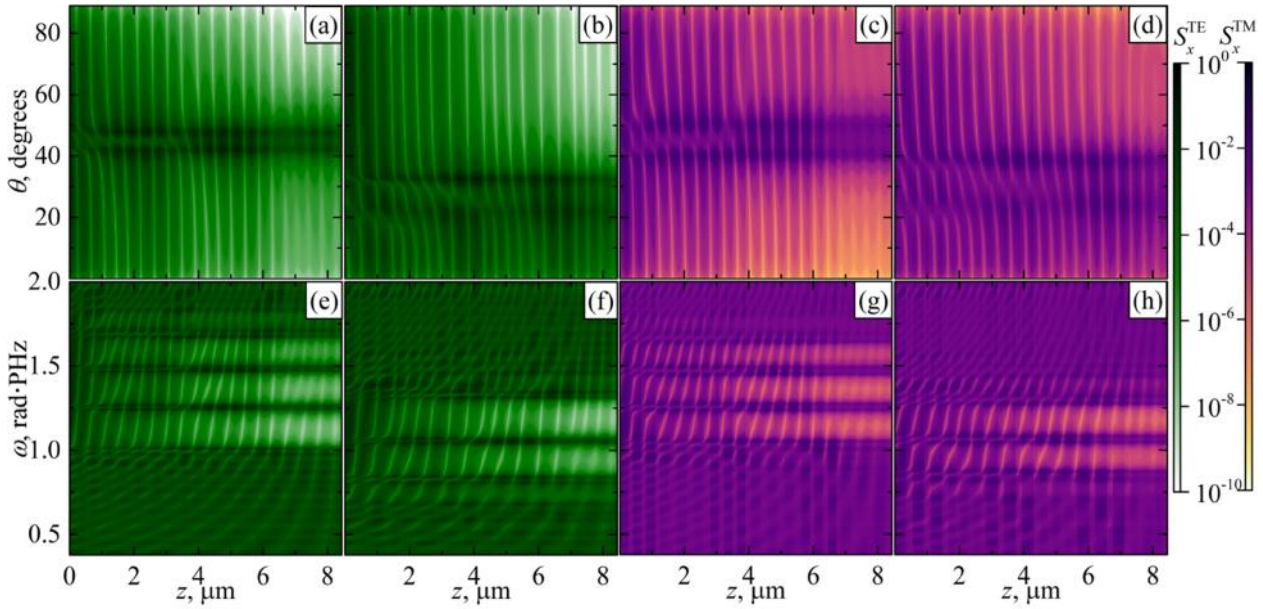

Fig. 4. The transverse intensity distributions (a-d): $S_x(\theta,z)$ [in erg/(μm²·s)] (in logarithmic scale); and (e-h): $S_x(\omega,z)$ [in erg/(μm²·s)] (in logarithmic scale)) in the structure $[(ST)^3(AZ)^3]^3$ with $^{a}_{0h}$ = 1.5 μm (μ_{0h} = 1.257 rad·PHz), $^{a}_{0l}$ = 2 μm (μ_{0l} = 0.942 rad·PHz) (a,c,e,g) and $^{a}_{0h}$ = 2 μm (μ_{0h} = 0.942 rad·PHz), $^{a}_{0l}$ = 1.5 μm (μ_{0l} = 1.257 rad·PHz) (b,d,f,h). The operating wavelength in (a-d) is λ = 1.5 μm; the incidence angle in (e-h) is θ = 45°. The first and the second columns show the TE-modes, the third and the forth columns show the TM-modes.

The dark areas in Fig. 4 represent high values of the magnitude S_x. One can see that the behavior of the intensity distribution depending on the frequency and incidence angle is determined by that of the corresponding transmission coefficients for this structure (see Figs. 3(f) and 3(o)). Indeed, the transverse flux is maximal at the angular and frequency positions of the intraband modes.

The regions with low values of S_x in Figs. 4(e) and 4(g) correspond to the PBG in the range of $1.0 < \mu < 1.7$ rad·PHz at $\theta = 45°$. It should be noted that for the TM-polarization, there are discontinuities in the distribution of the energy flux density due to jumps of the refractive index values at the boundaries between the layers (for details, see Ref. [26]). It is also worth noting that, even in the PBG, where the transmittivity $T \to 0$, the flux is still present in the structure, although its amplitude is very small: $S_x \sim 10^{-6} - 10^{-9}$ erg/(μm²·s).

To specify the dependence of the energy fluxes on the choice of the PBG centers $^{a}_{0h}$ and $^{a}_{0l}$, we carried out similar calculations for the case of permutation of their values $^{a}_{0h} \leftrightarrow {}^{a}_{0l}$, so that $^{a}_{0h}$ = 2 μm, $^{a}_{0l}$ = 1.5 μm. Overall, with this change [see Figs. 4(b), 4(d), 4(f), 4(h)], the flux distribution varies similarly to the transmission spectra of the corresponding structure [see Figs. 3(f) and 3(h) for TE- and Figs. 3(o) and 3(q) for TM-polarizations, respectively]. However, at the fixed operating wavelength ^{a} = 1.5 μm [μ = 1.257 rad·PHz, Figs. 4(b) and 4(d)] the flux distributions turn out to be more diffuse with less pronounced PBGs for both polarizations due to the fact that the transmission bands are broader at this wavelength than in the previous case [see e.g. Figs. 3(f) and 3(h)]. At the fixed incidence angle [Figs. 4(f) and 4(h)], the PBG exhibits a red-shift (towards the low-frequency region [0.8–1.25] rad·PHz).

C. Integral and partial linear powers

Let's consider the peculiarities of integral and partial linear power of the PC. The integral linear power P_{int} of the electromagnetic wave transmitted through the structure $[(ST)^3(AZ)^3]^3$, is presented as

$$P_{\text{int}} = \int_0^L S_x(z)dz \,. \qquad (3)$$

Figure 5 shows the integral linear power P_{int} as function of the incidence angle ¯ and angular frequency μ. The vertical dotted lines denote the frequencies corresponding to the PBG centers of the high- and low-optical-contrast subcells. The $P_{int}(\mu, ¯)$ spectra

mostly repeat the shape of the corresponding transmission spectra [see Figs. 3(f) and 5(a), 3(o) and 5(b), 3(h) and 5(c), 3(q) and 5(d)]. Note, however, that a certain minimum value of $P_{int} \neq 0$ can exist even in the PBG. The highest values of the P_{int} are localized at the defect modes inside the PBG, as well as in the transmission peaks closest to the PBG boundaries. The linear power in the passband modes (beyond the PBG) are clearly distinguished at the incidence angles approximately $\bar{} > 30°$ for TE-modes [Figs. 5(a) and 5(c)], whereas in the case of TM-polarization the passband modes flatten and are only slightly distinguishable in the range $30° < \bar{} < 60°$ [Figs. 5(b) and 5(d)].

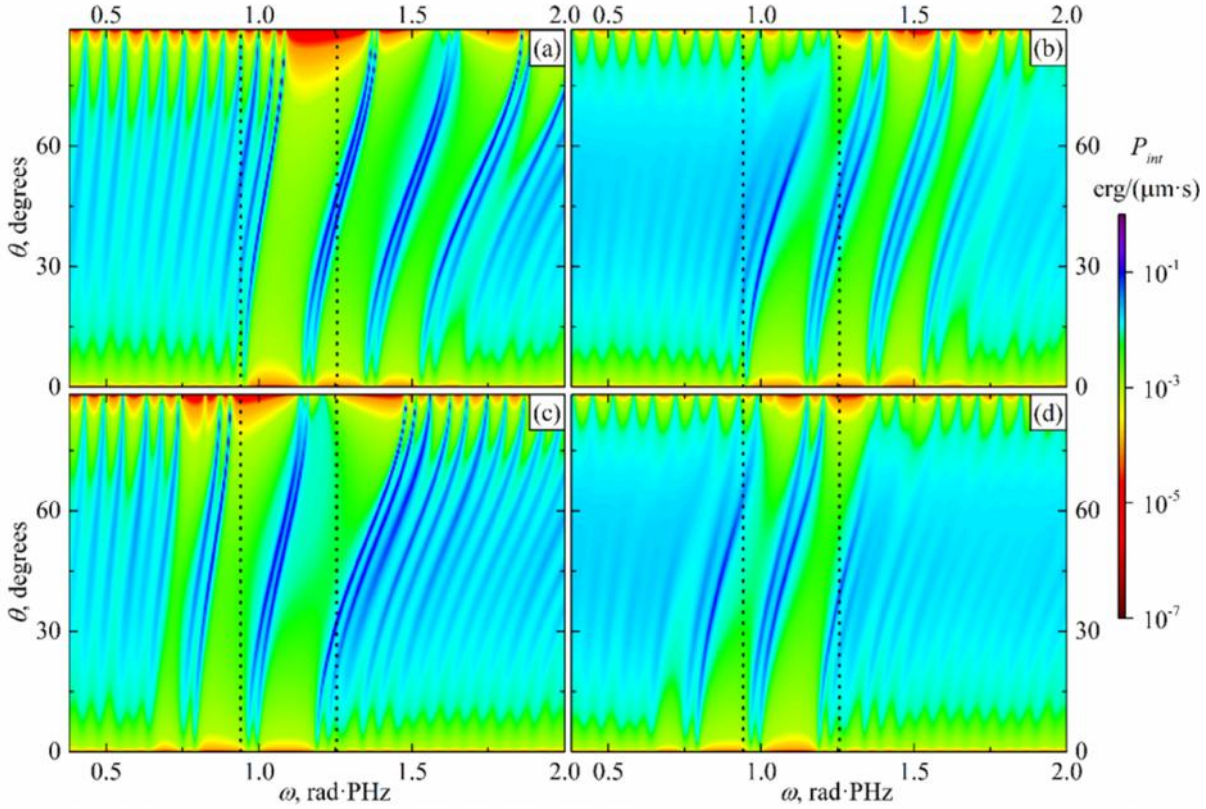

Fig. 5. The integral linear power in the structure $[(ST)^3(AZ)^3]^3$ as function of the incidence angle $\bar{}$ and frequency μ for $a_{0h} = 1.5$ μm, $a_{0l} = 2$ μm [(a) and (b)] and $a_{0h} = 2$ μm, $a_{0l} = 1.5$ μm [(c) and (d)]. The left and right columns show the TE- and TM-modes, respectively.

Partial linear power P_j [erg/(μm·s)] are defined as the sum of all the fluxes in each layer of type j (each of which is calculated by integrating the intensity distribution $S_x(z)$ within the boundaries of the corresponding individual layer):

$$P_j = \sum_X \int_{z_{left}}^{z_{right}} S_x(z)dz\,, \qquad (4)$$

where X is the total number of layers of the type j (j = S, T, A, Z), z_{left} and z_{right} are left- and right-hand-side boundaries of the j-layer. For instance, the partial flux P_S is the sum of the fluxes in all the layers S. The sum of all partial fluxes gives the total flux $P_{int} = \sum_j P_j$.

Figures 6 and 7 show the reduced partial linear power (P_j/P_{int}) in the structure $[(ST)^3(AZ)^3]^3$ for $a_{0h} = 1.5$ μm, $a_{0l} = 2$ μm (Fig. 6) and $a_{0h} = 2$ μm, $a_{0l} = 1.5$ μm (Fig. 7). From these figures one can see how the layers of each type contribute to the total energy flux at various frequencies and incidence angles for both polarizations. As follows out from Fig. 6, the major part of the power in the S layers is localized outside the PBG for both polarizations. On the other hand, most of the power corresponding to the intraband modes is localized in the layers A for TE-polarized mode [see Fig. 6(c)] and in the layers Z for the mode of TM-polarization [see Fig. 6(h)]. Such behavior can be explained by the fact that, in this case, the intraband modes of the structure are due to presence of the subcells $(AZ)^3$ (as periodic defects) inside the regular structure $(ST)^9$ which forms the PBG.

With the permutation of the values of the wavelengths of the PBG centers of the subcells (Fig. 7), the linear power distribution over the subcell layers changes. Indeed, in the PC with $a_{0h} = 2$ μm and $a_{0l} = 1.5$ μm, the linear power of the electromagnetic wave corresponding to the intraband modes is mostly localized in the layers Z for the TE-mode [Fig. 7(d)] and in the layers A for the TM-mode [Fig. 7(g)].

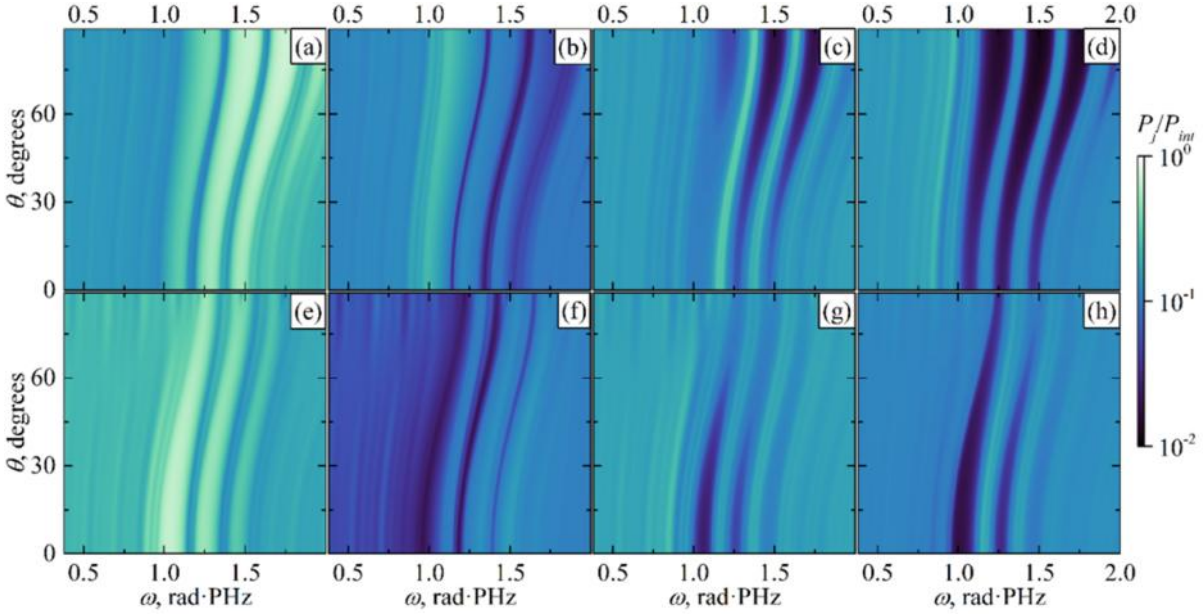

Fig. 6. Reduced partial linear powers P_j/P_{int} in the layers S, T, A, and Z (from the left to the right, the 1st, the 2nd, the 3rd, and the 4th columns, respectively) in the structure $[(ST)^3(AZ)^3]^3$ for the TE- and TM- modes (the top and the bottom rows, respectively). The PBG center wavelengths are $a_{0h} = 1.5$ μm, $a_{0l} = 2$ μm.

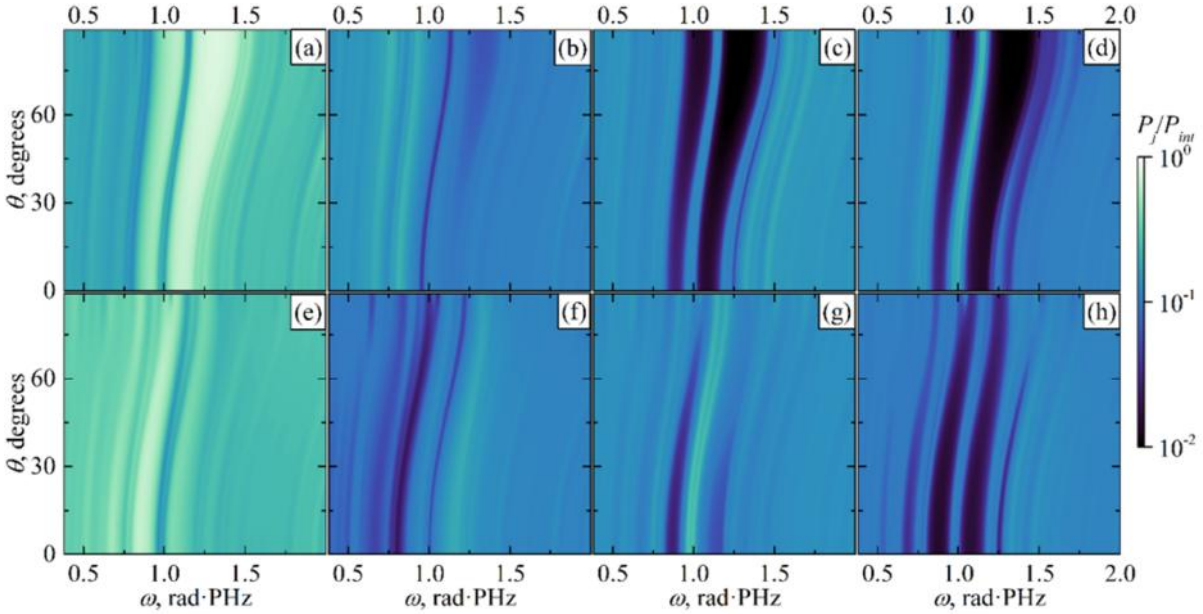

Fig. 7. The same as in Fig. 6 except for $a_{0h} = 2$ μm, $a_{0l} = 1.5$ μm.

4. POTENTIAL APPLICATIONS

Before discussing the potential applications of three-periodic PCs, it is worth to emphasize that the optical properties of the considered structures from the ***h-l-*** subgroup also characterize the other PCs of the ***hl*** group, i.e., the structures $[(ST)^N(AZ)^M]^K$, $[(ST)^N(ZA)^M]^K$, $[(TS)^N(AZ)^M]^K$, and $[(TS)^N(ZA)^M]^K$. As shown above, the transmission and energy flux spectra of three-periodic PCs can be adjusted *via* the choice of the PBG center wavelengths of the low- and high-optical-contrast subcells (which in practice is achieved by specifying the thicknesses of the constituent layers). Thus, one can configure the transmission spectrum of the structure in order to obtain a single transmission mode inside the PBG for each polarization at the fixed wavelength for all range of the incidence angles. Such a structure can act as a polarization-sensitive angle sensor with the given accuracy, or distributed Bragg reflector, or Fabri-Pérot filter [48]. For practical purpose we choose a PC of the structure $[(ST)^7(AZ)^1]^5$ which possesses a single transmission peak for both TE- and TM-modes.

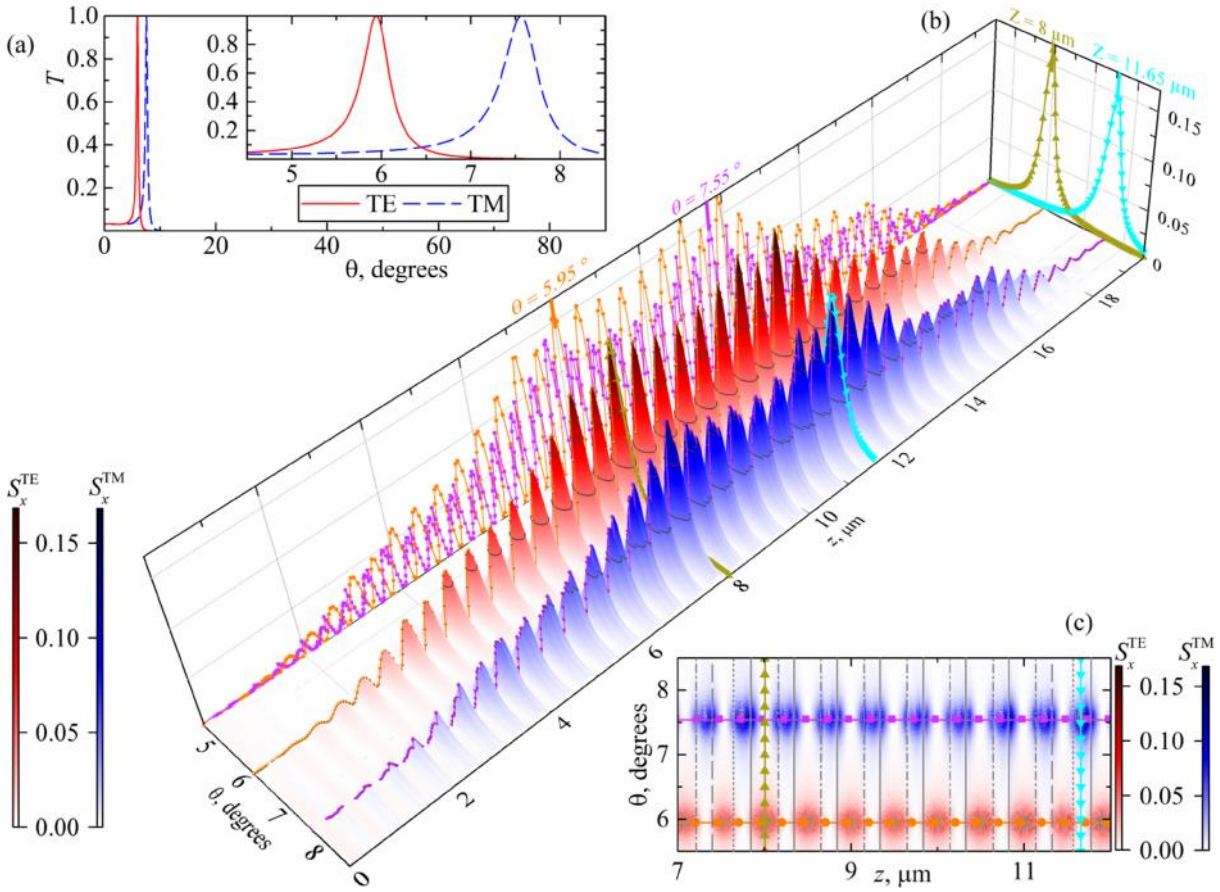

Fig. 8. (a) Transmission spectra of the TE- and TM-modes as functions of the incidence angle ¯; (b) the energy flux S_x (in [erg/(μm²·s)]) as function of the incidence angle and spatial coordinate z for the TE- modes (the shades of red) and the TM- modes (the shades of blue). The orange and purple dots indicate the envelopes of S_x for TE- and TM-modes (at fixed angles $\theta = 5.95°$ and 7.55°, respectively); (c) Distribution of the energy flux (in [erg/(μm²·s)]) of the TE- and TM-modes (top-view) in the layers of the structure $[(ST)^7(AZ)^1]^5$ for $a_{0h} = 1.8$ μm, $a_{0l} = 1.72$ μm. All calculations are carried out for the operating wavelength $a = 1.55$ μm.

Figure 8(a) shows the transmission spectra of the structure $[(ST)^7(AZ)^1]^5$ at the operating wavelength $a = 1.55$ μm. When specifying the layer thicknesses constituting the structure with the PBG centers of the low- and high-optical-contrast subcells at the wavelengths $a_{0h} = 1.8$ μm and $a_{0l} = 1.72$ μm (so that $l_S = 0.312$ μm, $l_T = 0.184$ μm, $l_A = 0.247$ μm, $l_Z = 0.204$ μm), the resulting PBG for each polarization has only one transmission peak within the whole range of the incidence angle. The full width at half maximum (FWHM) of the transmission mode is about 0.5°, and the angular distance (difference in the incidence angles) between the transmission peaks of different polarizations is about 1.5°. Although FWHM of the transmission peaks of the ternary PCs can be more narrow, the angular distance between the peaks in the three-periodic structure is about 5 times larger (cf. Ref. [27]), thus the modes in the three-periodic PC can be easily distinguished.

The transverse energy flux S_x distribution over the PC's length at different incidence angles is shown in Fig. 8(b) for the TE- and TM-modes. We made the cross-sections $[S_x(\theta, z = \text{const})]$ at the coordinates $z = 8$ μm and at $z = 11.65$ μm for TE- and TM-modes (the mustard up-pointing triangles and the cyan down-pointing triangles). These coordinates correspond to the maximal values of S_x in the structure (see the $S_x(\theta)$-plane).

On the other hand, the energy flux distribution $S_x(\theta = \text{const}, z)$ demonstrates several interesting peculiarities [see the orange (filled circles) and the purple (filled squares) lines in Fig. 8(b), $S_x(z)$-plane]. First, the peaks of the S_x of the TM-mode are on average somewhat lower than those of the TE-mode. Second, the "checkerboard" alternation of the peaks for the TE- and TM-modes inside the structure is well pronounced. Indeed, the position of the S_x maxima of the TE-mode coincide with the position of the S_x minima of the TM-mode. The third, the peaks of S_x for both TE- and TM-modes increase in value with the increasing z-coordinate until approximately the center of the PC, where they reach a maximum.

Figure 8(c) shows the distribution of the energy flux of TE- and TM-modes in the central part of the structure (7 μm < z < 12 μm). The solid and dash-dotted vertical lines mark the left-hand-side boundaries of the layers S and T of the high-optical-contrast subcell, and dashed and dotted lines mark the left-hand-side boundaries of the layers A and Z of the low-optical-contrast subcell, respectively. Inside the subcell $(ST)^7$, the peaks of S_x^{TE} are

localized in the S layers, whereas S_x^{TM} peaks are localized in the T layers. Inside the subcell (AZ)[1], the peak of S_x^{TE} is in the A layer and the peak of S_x^{TM} is in the Z layer. Moreover, for the TE-mode, the peaks of S_x are localized in the centers of the layers and practically do not spread beyond. In the case of TM-mode, due to the discontinuity of the fields at the boundaries, the peaks of the energy flux are bifurcated or split.

Taking into account the considered S_x picture, we can propose devices operating on the lateral surface of the PC. The structure can function as a polarization splitter which carries out the spatial splitting of the energy fluxes (i.e. peaks alternation) of TE- and TM-modes on the side surface of the PC (along the *z*-axis).

It should be noted that the principle of the proposed devices do not require high laser fields and the considered materials forming the multiperiodic structure are lossless in the near-IR regime. Thus, the heating in the system is negligibly small. On the other hand, the change of the refractive indices of the materials with temperature is about 10^{-5}-10^{-6} per 1 K [49]. So, all the discussed above optical properties of the system remain stable for small changes of temperature.

5. CONCLUSIONS

We performed an analysis of the spectral and energy characteristics of TE- and TM-modes in the dielectric three-periodic 1D PC structures of the type $[(SiO_2/TiO_2)^N(Al_2O_3/ZrO_2)^M]^K$, Such PCs have the broadest PBG among all the possible combinations of the above-mentioned layers forming a four-component three-periodic PC.

We have shown that the photonic bandgaps of such PC is formed by the spectral properties of the high-optical-contrast subcells, whereas the low-optical-contrast subcells act as complex defect layers and ensure existence and position of the inside-bandgap modes. Also we have studied peculiarities of the energy and power fluxes of TE- and TM-polarized waves in the structure. Based on this analysis, we can talk about the possibility of forming a certain distribution of the energy flux via: (i) selecting the numbers of the sub-periods *M* and *N* and super-period *K,* (ii) adjusting the layer thicknesses, i.e. modification of the corresponding positions of the photonic bandgap centers, (iii) changing the input angle, (iv) changing the wavelength, and (v) switching the polarization of the incident electromagnetic wave.

The considered structures have an advantage over the ternary PCs (on the base of oxides TiO_2, SiO_2, and Al_2O_3). The angular distance between the transmission peaks for the modes of TE- and TM-polarizations is shown to be about 1.5° that is five times more than that in the ternary PC. It means that the modes of the three-periodic PCs can be easily distinguished which can be put in the base of their practical application in polarization-sensitive splitters or detectors. Besides, three-periodic PCs can be used for designing high precision input-output devices (couplers) of near-infrared regime (for example, into optical fiber) through the lateral surface of the PC. Adjustable accuracy of the shift of the transmission mode in the angle or frequency can also be useful when working with laser sources (distributed-feedback lasers).

Funding. Russian Foundation for Basic Research (RFBR) (19-42-730008); Conseil Régional de Bretagne, France (SPEACS); Programme PAUSE of Collège de France; the Ministry of Higher Education and Science of the Russian Federation (Project "Development of comb-spectrum generators for applications in microwave photonics, spectroscopy, and high-speed data processing").

Disclosures. The authors declare no conflicts of interest.

References

[1] Shen H, Wang Z, Wu Y and Yang B 2016 One-dimensional photonic crystals: fabrication, responsiveness and emerging applications in 3D construction *RSC Adv.* **6** 4505–20

[2] Bellingeri M, Chiasera A, Kriegel I and Scotognella F 2017 Optical properties of periodic, quasi-periodic, and disordered one-dimensional photonic structures *Opt. Mater. (Amst).* **72** 403–21

[3] Mitra S, Biswas T, Chattopadhyay R, Ghosh J, Bysakh S and Bhadra S K 2016 Safe and simple detection of sparse hydrogen by Pd-Au alloy/air based 1D photonic crystal sensor *J. Appl. Phys.* **120** 173102–8

[4] Le N D and Nguyen-Tran T 2020 Simulation of coupling optical modes in 1D photonic crystals for optoelectronic applications *J. Sci. Adv. Mater. Devices* **5** 142–50

[5] Ramanujam N R, Amiri I S, Taya S A, Olyaee S, Udaiyakumar R, Pasumpon Pandian A, Joseph Wilson K S, Mahalakshmi P and Yupapin P P 2019 Enhanced sensitivity of cancer cell using one dimensional nano composite material coated photonic crystal *Microsyst. Technol.* **25** 189–96

[6] Nouman W M, Abd El-Ghany S E S, Sallam S M, Dawood A F B and Aly A H 2020 Biophotonic sensor for rapid detection of brain lesions using 1D photonic crystal *Opt. Quantum Electron.* **52** 287

[7] Abadla M M and Elsayed H A 2020 Detection and sensing of hemoglobin using one-dimensional binary photonic crystals comprising a defect layer *Appl. Opt.* **59** 418

[8] Hao K, Wang X, Zhou L, Yang S, Zhang J, Wang Y and Li Z 2020 Design of one-dimensional composite photonic crystal with high infrared reflectivity and low microwave reflectivity *Optik (Stuttg).* **216** 164794

[9] Celanovic I, O'Sullivan F, Ilak M, Kassakian J and Perreault D 2004 Design and optimization of one-dimensional photonic crystals for thermophotovoltaic applications *Opt. Lett.* **29** 863–5

[10] Pankin P S, Wu B R, Yang J H, Chen K P, Timofeev I V. and Sadreev A F 2020 One-dimensional photonic bound states in the continuum *Commun. Phys.* **3** 1–8

[11] Tolmachev V A, Perova T S and Berwick K 2006 Design of one-dimensional composite photonic crystals with an extended photonic band gap *J. Appl. Phys.* **99** 033507(5pp)

[12] Chen G and Yu H 2014 The enlargement of high reflectance range in ultra-narrow bandpass filter with disordered one-dimensional photonic crystal *J. Appl. Phys.* **115** 033114–6

[13] Glukhov I A, Dadoenkova Y S, Bentivegna F F L and Moiseev S G 2020 Deterministic aperiodic photonic crystal with a 2D array of metallic nanoparticles as polarization-sensitive dichroic filter *J. Appl. Phys.* **128** 053101

[14] Dadoenkova N N, Panyaev I S, Sannikov D G, Dadoenkova Y S, Rozhleys I A, Krawczyk M and Lyubchanskii I L 2016 Complex waveguide based on a magneto-optic layer and a dielectric photonic crystal *Superlattices Microstruct.* **100** 45–56

[15] Dadoenkova Y S, Lyubchanskii I L, Lee Y P and Rasing T 2012 Electric Field Controlled Optical and Magneto-Optical Effects at Light Transmission Through a One-Dimensional Magnetic Photonic Structure with Complex Defect Layer *J. Magn. Soc. Japan* **36** 32–5

[16] Panyaev I S, Dadoenkova N N, Dadoenkova Y S Y S, Rozhleys I A, Krawczyk M, Lyubchanskii I L and Sannikov D G 2016 Four-layer nanocomposite structure as an effective optical waveguide switcher for near-IR regime *J. Phys. D. Appl. Phys.* **49** 435103(10pp)

[17] Panyaev I S, Dadoenkova N N, Dadoenkova Y S, Rozhleys I A, Krawczyk M, Lyubchanskii I L and Sannikov D G 2016 Optical

properties of a four-layer waveguiding nanocomposite structure in near-IR regime *Opt. Quantum Electron.* **48**
[18] Kłos J W, Krawczyk M, Dadoenkova Y S, Dadoenkova N N, Lyubchanskii I L, Klos J W, Krawczyk M, Dadoenkova Y S, Dadoenkova N N, Lyubchanskii I L, Kłos J W, Krawczyk M, Dadoenkova Y S, Dadoenkova N N and Lyubchanskii I L 2014 Photonic-magnonic crystals: Multifunctional periodic structures for magnonic and photonic applications *Journal of Applied Physics* vol 115 pp 174311–2
[19] Dadoenkova Y S, Dadoenkova N N, Lyubchanskii I L, Klos J W and Krawczyk M 2016 Confined states in photonic-magnonic crystals with complex unit cell *J. Appl. Phys.* **120** 073903–9
[20] Klos J W, Krawczyk M, Dadoenkova Y S, Dadoenkova N N and Lyubchanskii I L 2014 Spin waves and electromagnetic waves in photonic-magnonic crystals *IEEE Trans. Magn.* **50** 2–5
[21] Dadoenkova Y S, Dadoenkova N N, Kłos J W, Krawczyk M and Lyubchanskii I L 2017 Goos-Hänchen effect in light transmission through biperiodic photonic-magnonic crystals *Phys. Rev. A* **96** 043804–6
[22] Dadoenkova Y S, Dadoenkova N N, Lyubchanskii I L, Klos J W and Krawczyk M 2017 Faraday Effect in Bi-Periodic Photonic-Magnonic Crystals *IEEE Trans. Magn.* **53** 1–5
[23] Narimanov E E 2014 Photonic hypercrystals *Phys. Rev. X* **4** 1–13
[24] Smolyaninova V N, Yost B, Lahneman D, Narimanov E E and Smolyaninov I I 2015 Self-assembled tunable photonic hyper-crystals *Sci. Rep.* **4** 5706(9 pp.)
[25] Zhukovsky S V., Orlov A A, Babicheva V E, Lavrinenko A V. and Sipe J E 2014 Photonic-band-gap engineering for volume plasmon polaritons in multiscale multilayer hyperbolic metamaterials *Phys. Rev. A - At. Mol. Opt. Phys.* **90** 013801(11 pp.)
[26] Chebykin A V., Babicheva V E, Iorsh I V., Orlov A A, Belov P A and Zhukovsky S V. 2016 Enhancement of the Purcell factor in multiperiodic hyperboliclike metamaterials *Phys. Rev. A* **93** 033855(9 pp.)
[27] Dadoenkova N N, Dadoenkova Y S, Panyaev I S, Sannikov D G and Lyubchanskii I L 2018 One-dimensional dielectric bi-periodic photonic structures based on ternary photonic crystals *J. Appl. Phys.* **123** 043101–8
[28] El-Amassi D M, Taya S A and Vigneswaran D 2018 Temperature sensor utilizing a ternary photonic crystal with a polymer layer sandwiched between Si and SiO2 layers *J. Theor. Appl. Phys.* **12** 293–8
[29] Shaban S M, Mehaney A and Aly A H 2020 Determination of 1-propanol, ethanol, and methanol concentrations in water based on a one-dimensional phoxonic crystal sensor *Appl. Opt.* **59** 3878
[30] Wu J and Gao J 2015 Analysis of Temperature-Dependent Optical Properties in 1D Ternary Superconducting Photonic Crystal with Mirror Symmetry *J. Supercond. Nov. Magn.* **28** 1971–6
[31] Lo S M, Hu S, Gaur G, Kostoulas Y, Weiss S M and Fauchet P M 2017 Photonic crystal microring resonator for label-free biosensing *Opt. Express* **25** 7046
[32] Aminifard S M and Sovizi M 2014 Simulation of transmitted spectrum in metallic photonic crystals by boundary element method *Opt. Commun.* **322** 1–7
[33] Girich A, Kharchenko A and Tarapov S 2019 Spectral Features of a Multi-Periodical Metamaterials *Proceedings of the International Conference on Advanced Optoelectronics and Lasers, CAOL* vol 2019-Septe (IEEE) pp 408–11
[34] Panyaev I S, Yafarova L R, Sannikov D G, Dadoenkova N N, Dadoenkova Y S and Lyubchanskii I L 2019 One-dimensional multiperiodic photonic structures: A new route in photonics (four-component media) *J. Appl. Phys.* **126** 103102 (11 pp.)
[35] Kuwabara M 2016 Photonic Crystals Fabricated by Sol–Gel Process *Handbook of Sol-Gel Science and Technology* (Springer International Publishing) pp 1–34
[36] Malitson I H 1965 Interspecimen comparison of the refractive index of fused silica *J. Opt. Soc. Am.* **55** 1205–9
[37] Malitson I H and Dodge M J 1972 Refractive Index and Birefringence of Synthetic Sapphire *J. Opt. Soc. Am.* **62** 1405
[38] Wood D L and Nassau K 1982 Refractive index of cubic zirconia stabilized with yttria *Appl. Opt.* **21** 2978–81
[39] Devore J R 1951 Refractive indices of rutile and sphalerite *J. Opt. Soc. Am.* **41** 416–9
[40] Dadoenkova N N, Dadoenkova Y S, Panyaev I S, Sannikov D G and Lyubchanskii I L 2018 Multi-periodic one-dimensional photonic crystals *Proceedings of the International Conference DAYS on DIFFRACTION* pp 1–6
[41] Inoue M, Baryshev A V. and Levy M 2013 *Magnetophotonics: From Theory to Applications* (Heidelberg: Springer-Verlag)
[42] Saleh B E A and Teich M C 2019 *Fundamentals of Photonics* vol II (New York: John Wiley & Sons)
[43] Zolotovskii I O, Panyaev I S and Sannikov D G 2019 Two ? frequency laser with distributed feedback formed by a space charge wave *Opt. Quantum Electron.* **51** 1–9
[44] Bianchi N J and Kahn L M 2020 Optical states in a 1D superlattice with multiple photonic crystal interfaces *J. Opt. (United Kingdom)* **22**
[45] Gong Q and Hu X 2014 *Photonic Crystals: Principles and Applications* (Pan Stanford)
[46] Ito T and Okazaki S 2000 Pushing the limits of lithography *Nature* **406** 1027–31
[47] Akhmanov S A and Nikitin S Y 2004 *Physical Optics* (Moscow: Nauka [in Russian])
[48] Mai H H 2020 Designing multilayer dielectric filter based on TiO2/SiO2 for fluorescence microscopy applications *Comput. Opt.* **44** 209–13
[49] Palik E D 1997 Thermo-Optic Coefficients *Handbook of Optical Constants of Solids, Vol.5* (New York: Elsevier) pp 115–261